Journal of Computational Applied Mechanics 2026, 57(2): 173-194

DOI: 10.22059/jcamech.2025.405184.1675

RESEARCH PAPER

Magnetic Hydrodynamic Flow and Heat Transfer of Williamson Nanofluids in a Porous Medium Impact of Chemical Reactions and Melting Effects

Muhammad Saad [a, *], Muhammad Sulaiman [a], Muhammad Fawad Khan [b], Ghaylen Laouini [c], Rashid Ashraf [d], Fahad Sameer Alshammari [e]

[a] *Department of Mathematics, Abdul Wali Khan University, Mardan, 23200, Mardan, Pakistan*
[b] *School of Information Technology and Systems, University of Canberra, Canberra ACT 2617, Australia*
[c] *College of Engineering and Technology, American University of the Middle East, Egaila 54200, Kuwait*
[d] *Scuola Internazionale Superiore di Studi Avanzati Via Bonomea 265, 34136 Trieste, Italy*
[e] *Department of Mathematics, College of Science and Humanities in Al-Kharj, Prince Sattam bin Abdulaziz University, Al-Kharj 11942, Saudi Arabia*

Abstract

Radiation and chemical reaction effects on the steady magnetohydrodynamic (MHD) boundary layer flow of Williamson nanofluid through a porous medium over a horizontally linearly stretching sheet are numerically investigated, incorporating coupled influences of melting heat transfer and nanoparticle dispersion. The governing partial differential equations are reduced to a system of nonlinear ordinary differential equations using similarity transformations and solved via the fourth-order Runge-Kutta (RK-4) method to generate reference datasets. A novel supervised machine learning framework, Feed-Forward Neural Network optimized with the Backpropagated Levenberg-Marquardt Algorithm (FFNN-BLMA), is proposed, trained on 1001 data points with 70% training, 15% validation, and 15% testing splits. The FFNN-BLMA yields exceptional predictive accuracy with absolute errors ranging from 10^{-8} to 10^{-10} across velocity $f'(\eta)$, temperature $\theta(\eta)$, and concentration $\phi(\eta)$, profiles, validated through 10-fold cross-validation, error histograms, regression analysis, and curve superposition. Parametric studies reveal that increasing the melting parameter M enhances velocity and reduces temperature, while the chemical reaction parameter γ diminishes concentration trends consistent with prior literature. Skin friction, Nusselt, and Sherwood numbers are computed to quantify engineering performance. The FFNN-BLMA outperforms traditional RK-4 and analytical methods in accuracy, convergence, and computational efficiency, establishing a robust, discretization-free paradigm for solving complex non-Newtonian multi-physics flow problems with potential extension to fractional-order systems.

Keywords: Melting heat transfer; Thermal radiation; Stretching surface; Williamson nanofluid; Machine learning; Chemical reaction; Artificial neural network

* Corresponding author. msaad.maths@awkum.edu.pk

1. Introduction

Nanofluids offer exceptional qualities such as high heat conductivity, reduced blockage in flow channels, homogeneity, and long-term stability because the nanoparticles are very small and have extremely large specific surface areas. Therefore, peristaltic pumps for the treatment of diabetes, solar collectors, pharmaceutical delivery methods, electronics cooling, and nuclear applications are just a few of the many possible uses for nanofluids. Zeng et al. [1] proposed the idea of using nanofluids to suspend liquids with very small particles. In their initial study on nanofluids, Alqahtani et al. [2] considered the issue of flow across a stretched sheet. The issue of nanofluid flow through a porous material across a horizontal plate and a naturally occurring convective boundary layer has been examined by Endalew et al. [3].

Numerous technical and industrial processes involve non-Newtonian fluids, including the mixing of food, the movement of chyme in the gut, blood, and plasma flow, mercury amalgam flow, and the lubrication of heavy oil and grease. Mabood et al. [4] used the homotopy analysis method (HAM) to four flow problems on a Williamson fluid, namely Blasius, Sakiadis, stretching, and stagnation points flows, to obtain a series solution. Megahed [5, 6] modelled a two-dimensional analysis of Williamson fluid flow across a stretched surface with linear and exponential components. For the time-independent MHD flow through a porous plate in a Williamson fluid, Maaitah et al. [7-9] discovered a series solution.

Non-Newtonian fluids are grouped property-wise as polar fluids, anisotropic fluids, visco-elastic fluids, visco-inelastic fluids, and micro-structured fluids. One of these visco-inelastic fluids is the Williamson fluid. The rheological characteristics of nanofluids have recently been ascertained using non-Newtonian modeling of nanofluid transport phenomena, even though nanofluids have traditionally been treated as Newtonian fluids. Non-Newtonian fluids with dispersed nanoparticles over a stretched sheet are the subject of several investigations. Khan et al. [10-12] nanoparticles of the Casson fluid model were studied based on the convective surface boundary conditions. A similar solution of the Casson nanofluid heat transfer through an exponentially expanding cylinder and the time-independent boundary layer flow was obtained by Prasad et al. [13-15]. The stress relaxation characteristics of the retardation ratio are visible in the Jeffrey fluid. Titiloye et al. [16-18] investigated the Jeffrey fluid model's steady flow when nanoparticles were present. Using a solar energy model, Gireesha et al. [19-21] investigated the MHD three-dimensional flow of Nano Jeffrey fluid, combining thermophoresis characteristics and Brownian motion. Shehzad et al. [22, 23] also studied the impact of nanoparticles on Jeffrey fluid's MHD on a stretched surface, considering convective boundary conditions for the concentration of nanoparticles and temperature. Abdullah Mohamed et al. [24-26] examined the mass and heat transfer of an inflexible Jeffrey nanofluid moving across a rapidly expanding region in two dimensions using hydromagnetic flow. The three-dimensional Oldroyd-B nanofluid flow over a bi-directional stretching sheet that produces and absorbs heat was studied by Lu et al. [27, 28] in terms of its free convective boundary layer. They explained the rheological behaviour of viscoelastic nanofluids using the Oldroyd-B fluid model. Hayat et al. [29, 30] developed a series of solutions regarding the viscoelastic nanofluid flow across a stretched cylinder with simultaneous impacts on mass and heat transfer using the homotopy analysis method (HAM), a well-known analytical approach. Kho et al. [31, 32] examined the effect of nanoparticles on two-dimensional fluid flow over a stretched sheet and Williamson fluid. In convective boundary conditions, Swain et al. [33] investigated the time-dependent flow of a suspended Maxwell fluid in nanoparticles over a stretched sheet as a function of a heat sink and source.

Over the last few years, both theoretical and experimental research have been conducted about the role of natural convection in the kinetics of heat transfer, accompanied by melting or solidification effects. Thermal engineering has a lot of potential uses in operations, including making silicon wafers, getting oil out of the ground, melting permafrost, magma solidification, getting geothermal energy, and thermal insulation, etc, all need to move heat through non-Newtonian fluids. Ren [34] was the first to describe the phenomena of ice melting in a warm air stream under steady conditions. Lienhard et al. [35], conducted experiments on laminar film condensation on a vertical melting surface. In a hydromagnetic forced convection flow on a horizontally extended plate under a transverse magnetic field, Sharma et al. [36] analyzed the effect of transverse magnetic field on hydromagnetic, forced convection flow with heat and mass transfer of a nanofluid over a horizontal stretching plate under the influence of melting and heat generation or absorption. The layer that separates a heated, laminar nanofluid flow parallel to a melting surface from a uniform free stream was examined by Endalew et al. [3]. In the presence of thermal radiation and an uneven heat source or sink, Prasanna kumara et al. [37] investigated the melting of a dusty fluid that was flowing across a stretched sheet around the MHD stagnation spot.

Heat and mass transfer study on fluids with chemical reaction effect over a stretching sheet has an important role in metallurgy and chemical engineering industries, such as food processing and polymer production. Moreover, coupled heat and mass transfer problems in the presence of chemical reaction are of importance in many processes

and have therefore received a considerable amount of attention in recent times. Possible applications can be found in processes such as drying, distribution of temperature and moisture over agricultural fields and groves of fruit trees, damage of crops due to freezing, evaporation at the surface of a water body, energy transfer in a wet cooling tower, and flow in a desert cooler, see Hasan [38].

Dash et al. [39] found an analytical solution to the steady stagnation points flow of the polar fluid in the boundary layer to a stretched surface in porous media, taking into account the effects of both the Soret and Dufour numbers as well as a first-order homogeneous chemical reaction. Sahu et al. [40] investigated the impact of chemical reactions and heat stratification on the mass and heat transport of free convective boundary layers of an electrically conducting fluid using a time-varying stretched sheet of fluid. Lv et al. [41] investigated the effects of time-dependent chemical reactions on the stagnation point flow and heat transmission of a nanofluid via a stretched sheet using numerical data. The boundary layer flow of nanofluids by mixed convection at a stagnation point over a permeable stretching/shrinking sheet exposed to a heat source/sink, chemical reaction, viscous dissipation, and thermal radiation was numerically investigated by Pal and Seth [42, 43].

Over the past two decades, a wealth of scholarly work has emerged, with researchers thoroughly exploring various architectures of artificial neural networks (ANNs) [41, 44, 45]. In contrast to conventional analytical techniques, such as the Homotopy Analysis Method (HAM) [41, 46], or standalone numerical schemes like the fourth-order Runge-Kutta (RK-4) method [41, 47], which often encounter convergence challenges and high computational demands in complex non-Newtonian nanofluid systems, the present study introduces a novel supervised machine learning framework, employing a Feed-Forward Neural Network optimized via the Backpropagated Levenberg-Marquardt Algorithm (FFNN-BLMA), for the numerical solution of a highly nonlinear system of ordinary differential equations describing magnetohydrodynamic (MHD) boundary layer flow of Williamson nanofluid through a porous medium over a linearly stretching sheet. This model integrates coupled effects of melting heat transfer, thermal radiation, and first-order chemical reactions. The proposed FFNN-BLMA utilizes RK-4-generated reference datasets for training, yielding exceptional accuracy with absolute errors in the range of 10^{-8} to 10^{-10} across velocity, temperature, and concentration profiles. This AI-based methodology obviates the requirements for discretization or differentiability assumptions, ensures robust generalization through 10-fold cross-validation and minimization of mean squared error, and facilitates comprehensive parametric sensitivity analysis (e.g., variations in melting parameter M and chemical reaction parameter γ) via error histograms, regression metrics, and superimposed solution curves. Consequently, the FFNN-BLMA approach represents a significant advancement in computationally efficient and reliable soft computing strategies for multi-physics nanofluid flow problems, with promising extensibility to fractional-order partial differential equations in diverse engineering applications [41, 48-50].

2. Nomenclature

MHD	Magnetohydrodynamics
MLP	Multilayer perceptron
ML	Machine learning
HAM	Homotopy analysis method
ANN	Artificial neural network
MSE	Mean squared error
ODE's	Ordinary differential equations
LM	Levenberg-Marquardt
AI	Artificial intelligence
FFNN	Feed-forward neural network
M	Melting parameter
T	Nanofluid temperature
v	Kinematic viscosity
k	Thermal conductivity
RK-4	Runge-Kutta method of order four
BLMA	Backpropagated Levenberg-Marquardt algorithm
Sh_x	Sherwood number
Nu_x	Nusselt number

C_f	Skin fraction coefficient
q_m	Surface mass flux
q_w	Surface heat flux
τ_w	Sheer stress
γ	Chemical reaction parameter
$f'(\eta)$	Velocity profile
$\theta(\eta)$	Temperature profile
$\phi(\eta)$	Concentration profile
k'	Permeability of the porous medium
k_0	Chemical reaction coefficient
C	Volumetric volume expansion coefficient
T_w	Temperature of the nanofluid near the wall
T_∞	Free stream temperature of the nanofluid
D_B	Brownian diffusion coefficient
D_T	Thermophoresis diffusion coefficient

3. Mathematical formulations

Examine the two-dimensional, continuous, incompressible Williamson nanofluid flow across a stretched surface with an embedded porous medium. A velocity ax stretches the plate along the x-axis, with the stretching parameter $a>0$. The flow structure is shown in Figure 1. The assumed values for temperature, fluid velocity, and concentration of nanoparticles near the surface, denoted as C_w, U_w, and T_w, respectively. Additionally, the melting surface temperature is denoted as T_m, and the free stream condition temperature is T_∞, where $T_\infty > T_m$. It is assumed that there is negligible viscous dissipation and minimal heat generation or absorption [51].

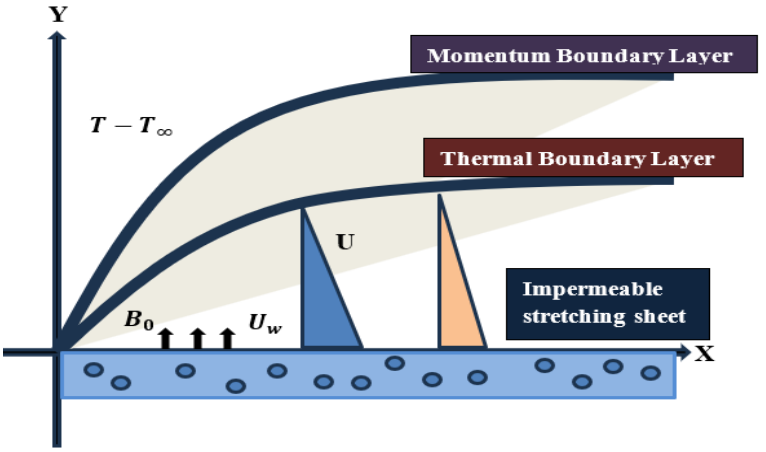

Figure 1. Diagrammatic representation of the movement of the boundary layer across a stretched sheet.

For the present problem, the basic equations that conserve momentum, mass, concentration, and energy for a steady nanofluid flow may be written as follows in Cartesian coordinates x and y [52].

$$\frac{\partial u}{\partial x}+\frac{\partial v}{\partial y}=0, \tag{1}$$

$$u\frac{\partial u}{\partial x}+v\frac{\partial u}{\partial y}=v\frac{\partial^2 u}{\partial y^2}+\sqrt{2}\,v_T\frac{\partial u}{\partial y}\frac{\partial^2 u}{\partial y^2}-\frac{\sigma\beta_0^2}{\rho}u-\frac{v}{k'}u, \tag{2}$$

$$u\frac{\partial T}{\partial x}+v\frac{\partial T}{\partial y}=\alpha_m\frac{\partial^2 T}{\partial y^2}+\tau\left[D_B\frac{\partial C}{\partial y}\frac{\partial T}{\partial y}+\frac{D_T}{D_\infty}\left(\frac{\partial T}{\partial y}\right)^2\right]-\frac{1}{(\rho c)_f}\frac{\partial q_r}{\partial y}, \tag{3}$$

$$u\frac{\partial C}{\partial x}+v\frac{\partial C}{\partial y}=D_B\frac{\partial^2 C}{\partial y^2}+\frac{D_T}{D_\infty}\frac{\partial^2 T}{\partial y^2}-k_0 C. \tag{4}$$

The matching boundary requirements are given by

$$u=U_w(x)=ax,\quad T=T_m,\quad C=C_w \quad \text{at} \quad y=0,$$
$$u=0,\quad T\to T_\infty,\quad C\to C_\infty \quad \text{as} \quad y\to\infty, \quad \text{and}$$

$$k\left(\frac{\partial T}{\partial y}\right)_{y=0}=\rho\left[\beta+c_s(T_m-T_0)\right]v(x,0). \tag{5}$$

The radiative heat flow may be written as follows when assessing radiation using the Rosseland approximation.

$$q_r=-\frac{4\sigma^*}{3k^*}\frac{\partial T^4}{\partial y}, \tag{6}$$

where the mean is the coefficient of absorption, denoted by k^* and the Stefan-Boltzmann constant is denoted by σ^*. It is believed that temperature changes within the flow are minor enough to use a truncated Taylor series around the free stream temperature T_∞, to approximate T^4 as a temperature-dependent linear function T. Higher-order components resulting from this approximation are disregarded.

$$T^4\approx 4T_\infty^3T-3T_\infty^4. \tag{7}$$

Replacing equations 6 and 7 in equation 3. It follows

$$u\frac{\partial T}{\partial x}+v\frac{\partial T}{\partial y}=\alpha_m\frac{\partial^2 T}{\partial y^2}+\tau\left[D_B\frac{\partial C}{\partial y}\frac{\partial T}{\partial y}+\frac{D_T}{D_\infty}\left(\frac{\partial T}{\partial y}\right)^2\right]+\frac{16\sigma^*T_\infty^3}{3k^*(\rho c)_f}\frac{\partial^2 T}{\partial y^2}. \tag{8}$$

The governing equations can be converted into ordinary differential equations using the ensuing similarity transformation.

$$\psi=(a\nu)^{1/2}xf(\eta),\quad \eta=\left(\frac{a}{\nu}\right)^{1/2}y,\quad \theta(\eta)=\frac{T-T_m}{T_\infty-T_m},\quad \phi(\eta)=\frac{C-C_w}{C_\infty-C_w}. \tag{9}$$

The definition of stream function ψ is such that $v=-\frac{\partial\psi}{\partial x},\quad u=\frac{\partial\psi}{\partial y}$.

Equation (1) is likewise satisfied with the help of the modifications mentioned above, and the following forms are taken by equations (2), (4), and (8), as well as the boundary condition (5).

$$f'''+ff''-(f')^2+\lambda f''f'''-(Q+k_p)f'=0, \tag{10}$$

$$\frac{(1+\frac{4}{3}R)\theta''}{Pr}+\left(f\theta'+N_b\phi'\theta'+N_t(\theta')^2\right)=0, \tag{11}$$

$$\phi''+Le\,f\phi'+\frac{N_t}{N_b}\theta''-\gamma\phi=0, \tag{12}$$

where the prime indicates derivatives for f, θ, and ϕ are functions of η. The corresponding boundary

condition will be as follows:

$$f'(0)=1,\quad Pr\,f(0)+M\theta'(0)=0,\quad \theta(0)=0,\quad \phi(0)=0,$$
$$f'(\infty)=0,\quad \theta(\infty)=1,\quad \phi(\infty)=1. \tag{13}$$

The local Sherwood number Sh_x, local Nusselt number Nu_x, and skin fraction coefficient c_f are examples of important physical variables that are defined as

$$Nu_x=\frac{xq_w}{k(T_\infty-T_m)},\quad Sh_x=\frac{xq_m}{D_B(C_\infty-C_w)},\quad c_f=\frac{\tau_w}{\rho U_w^2}, \tag{14}$$

where the surface mass flux (q_m), surface heat flux (q_w), and sheer stress (τ_w), are provided by

$$q_w=-k\frac{\partial T}{\partial y},\quad q_m=-D_B\frac{\partial C}{\partial y},\quad \tau_w=\mu\left(\frac{\partial u}{\partial y}+\frac{T}{\sqrt{2}}\left(\frac{\partial u}{\partial y}\right)^2\right)\quad \text{at}\quad y=0. \tag{15}$$

With the help of the non-dimensional variables, it follows to

$$Nu_x(Re_x)^{1/2}=-\theta'(0),\quad C_f(Re_x)^{1/2}=f''(0)+\frac{\lambda}{2}\left(f''(0)\right)^2,\quad Sh_x(Re_x)^{1/2}=-\phi'(0) \tag{16}$$

where $Re_x=\frac{XU_w(X)}{\nu}$ is the local Reynolds number.

4. Methodology

Let's begin by outlining the fundamental construction and operation of a feed-forward neural network (FFNN) architecture, given in Figure 2, before delving into the optimization process for training neurons in it [51].

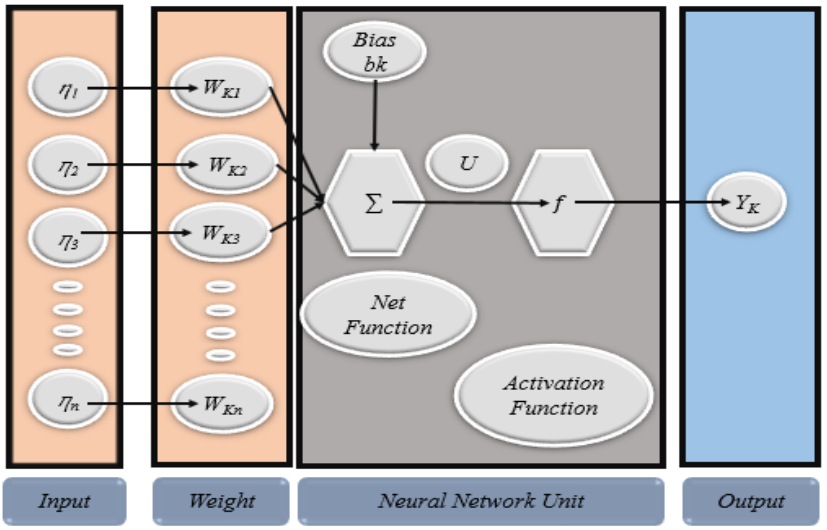

Figure 2. An artificial neural network with a simple design consisting of input, hidden, and output layers.

4.1. Artificial Neural Networks (ANNs)

An artificial neural network is an abbreviation for an architecture that is parallel in nature and is inspired by the method in which the central nervous system processes information. A neural network is a system of interconnected computers that may be used to simulate brain activity and learning on a computer. Neural networks were conceptualized by neuroscientists studying neurons in human and animal brains while performing related studies. Artificial intelligence research and development aims to give computing equipment the capacity to comprehend information and draw conclusions similar to those of humans. An artificial neural network, a subfield of artificial

intelligence, is a sophisticated concept in this area. A feed-forward neural network with many layers, or MLP, is the most often used type of artificial neural network (ANN) architecture, although there are many other types as well [41]. An ANN's structure may be expressed numerically as

$$W(\eta)=\sum_{j=1}^{N}\hat{\alpha}_j\, f\left(\hat{b}_j\eta+\hat{c}_j\right), \tag{17}$$

where weights or neurons optimized through the optimization process are represented by $\hat{\alpha}_j$, $\hat{b}_j$, and $\hat{c}_j$ the activation function used in this study is the tangent sigmoid, represented by *f,* and explained as below:

$$f(\eta)=\frac{e^{\eta}-e^{-\eta}}{e^{\eta}+e^{-\eta}}. \tag{18}$$

The activation function known as the hyperbolic tangent is commonly abbreviated as "Tanh" (or occasionally "tanh" or "tanh"). It displays a curve with an S-shape that resembles the sigmoid activation function. This method returns values between -1 and 1 and accepts any real value as input.

4.2. Collection of Data

This section discusses the dataset used for the solutions' supervised learning. The investigation examined various scenarios to explore how temperature, concentration, and velocity affect performance. The different scenarios explored in this study are presented in Table 1. In each of these situations, the dataset for supervised learning was constructed using the Runge-Kutta algorithm of order 4 and the "ND-Solve" numerical solver in Mathematica.

Table 1. Interpretation of the scenario, along with cases, for an RK-4 model.

		Physical quantities									
Scenario	Cases	Q	Kp	R	Pr	Nb	Nt	Le	γ	λ	M
1	C1	0.3	2	0.01	3.2	0.45	0.45	10	0.01	0.2	0.5
	C2	0.3	2	0.01	3.2	0.45	0.45	10	0.01	0.2	1
	C3	0.3	2	0.01	3.2	0.45	0.45	10	0.01	0.2	1.5
	C4	0.3	2	0.01	3.2	0.45	0.45	10	0.01	0.2	2
2	C1	0.3	2	0.01	3.2	0.45	0.45	1	0.01	0.2	0.5
	C2	0.3	2	0.01	3.2	0.45	0.45	1	0.01	0.2	1
	C3	0.3	2	0.01	3.2	0.45	0.45	1	0.01	0.2	1.5
	C4	0.3	2	0.01	3.2	0.45	0.45	1	0.01	0.2	2
3	C1	0.3	2	0.01	3.2	0.45	0.45	10	0	0.2	0.5
	C2	0.3	2	0.01	3.2	0.45	0.45	10	0.05	0.2	0.5
	C3	0.3	2	0.01	3.2	0.45	0.45	10	0.1	0.2	0.5
	C4	0.3	2	0.01	3.2	0.45	0.45	10	0.2	0.2	0.5

4.3. ANN with Levenberg-Marquardt Algorithm

The field of machine learning that studies how machines can be taught to learn from the data provided to them is known as machine learning. The computer method based on machine learning algorithms is an example of learning by example that does not presuppose the existence of any model. These algorithms are used in artificial intelligence (AI). When there are more data points available for learning, these algorithms are able to make dynamic improvements to their performance. Moreover, Figure 3 illustrates the operational stages of the method (FFNN-BLMA), which will be discussed below.

- ✓ The initial dataset is generated by a numerical solver, such as the Runge-Kutta method, for the supervised procedure of the machine learning algorithm. This step is used to determine how well the model performs on real-world datasets.
- ✓ Furthermore, using MATLAB's "NFTOOL," the feed-forward architecture of an artificial neural network (FFNN) with ten neurons in the hidden layer is constructed, as seen in Figure 4. The target data

for the FFNN is the 1001-point dataset that was acquired in the first step. The FFNN model uses 70% of the dataset for training, 15% for validation, and 15% for testing.

- ✓ The mean squared error (MSE) is often used as the objective function in a Feedforward neural network (FFNN). The MSE measures the average difference between the predicted output and actual output. The objective is to minimize this error during the training process to improve the model's accuracy. E is the mathematical expression for the fitness function.

$$E = \frac{1}{m}\sum_{i=1}^{m}\left(\hat{y}_i - y_i\right)^2, \tag{19}$$

where, y_i is the predicted target value of the i^{th} sample in a solution dataset, and its output varies between input variables.

- ✓ The Levenberg–Marquardt algorithm is an optimization method used to minimize a non-linear least-squares function. It is a combination of the gradient descent and the Gauss–Newton method, and uses a damping parameter to control the trade-off between exploration and exploitation. It is widely used in applications such as curve fitting, training artificial neural networks, and solving nonlinear systems of equations. It is an efficient method for finding the optimal weights associated with the predicted solution in Equation (19). This algorithm adjusts the weights until the error between the predicted and actual solution is minimized. Therefore, [41] presents step-by-step mathematical procedures for implementing the LM algorithm.

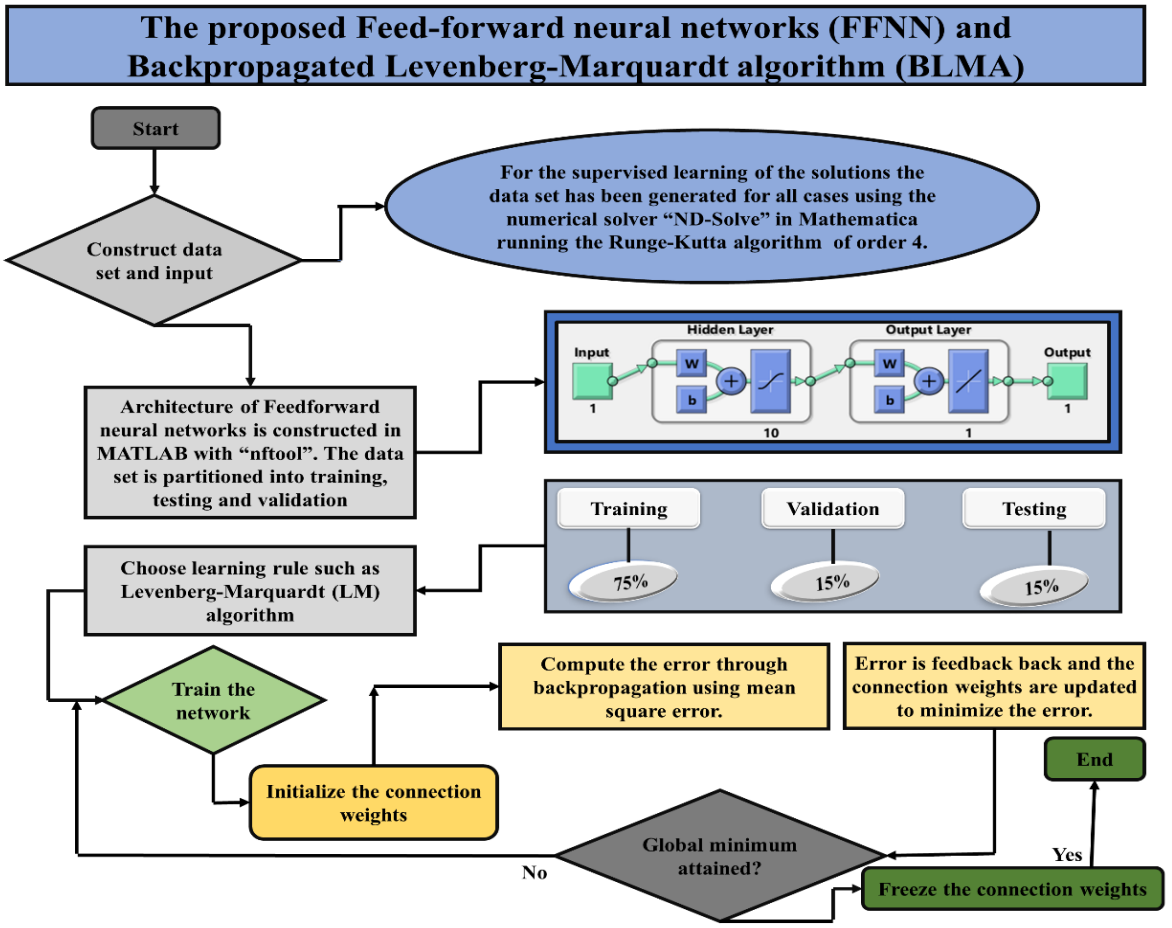

Figure 3. The following operational phases guided the development of the algorithm.

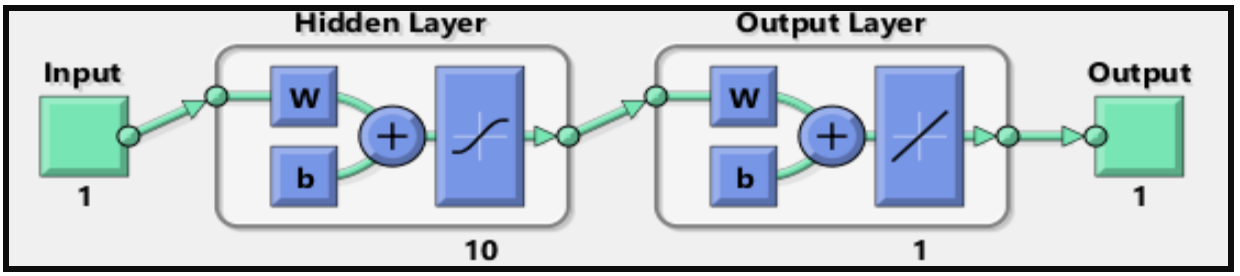

Figure 4. The neural network's feed-forward supervised learning design.

5. Results and Discussion

The outcomes presented in this section are obtained using the Feed-Forward Neural Network with Backpropagated Levenberg-Marquardt Algorithm (FFNN-BLMA) to investigate the coupled influences of melting heat transfer, magnetohydrodynamic (MHD) boundary layer flow, and Williamson nanofluid dynamics within a porous medium under the effect of first-order chemical reactions. Neural network weights are optimized via the Levenberg-Marquardt algorithm [41]. The nonlinear system of ordinary differential equations (10) – (12), subject to the boundary conditions in Eq. (13), is solved to determine the velocity $f'(\eta)$, temperature $\theta(\eta)$, and concentration $\phi(\eta)$, profiles. Specific numerical values are assigned to the governing parameters to systematically explore the effects of key flow-regulating factors, particularly the melting parameter M and the chemical reaction parameter γ. The resulting velocity, temperature, and concentration distributions are presented graphically to elucidate the physical behaviour of the system.

A quantitative comparison between the proposed FFNN-BLMA method and the reference RK-4 solutions for the velocity profile $f'(\eta)$, under varying melting parameters $M = 0.5,1,1.5,2,$ as shown in Table 2. The independent variable η is listed in the first column. The RK-4 results are reported in the second, fifth, eighth, and eleventh columns, while the corresponding FFNN-BLMA predictions are given in the third, sixth, ninth, and twelfth columns, respectively. This structured comparison clearly demonstrates the influence of the melting parameter on the velocity distribution and validates the neural network model's high fidelity.

Table 2. The *f'(η)* outputs for the proposed method and compared with the reference solution over different M.

f'(η)	*RK-4*	*BLMA*	*Error*	*RK-4*	*BLMA*	*Error*	*RK-4*	*BLMA*	*Error*	*RK-4*	*BLMA*	*Error*
	M=0.5	*M=0.5*		*M=1*	*M=1*		*M=1.5*	*M=1.5*		*M=2*	*M=2*	
0	*1*	*0.99990779*	*9.2×10^{-05}*	*1*	*0.99990917*	*9.0×10^{-05}*	*1*	*0.99982592*	*0.00017408*	*1*	*0.99985152*	*0.00014848*
0.5	*0.42105648*	*0.42103629*	*2.0×10^{-05}*	*0.42414881*	*0.42413114*	*1.7×10^{-05}*	*0.42723586*	*0.42722512*	*1.0×10^{-05}*	*0.43031724*	*0.43028794*	*2.93×10^{-05}*
1	*0.17335037*	*0.17335895*	*8.5×10^{-06}*	*0.17597006*	*0.17598259*	*1.2×10^{-05}*	*0.17860528*	*0.17862961*	*2.4×10^{-05}*	*0.18125559*	*0.18128307*	*2.75×10^{-05}*
1.5	*0.07063365*	*0.07064118*	*7.5×10^{-06}*	*0.07226051*	*0.07226 4*	*3.4×10^{-06}*	*0.07390985*	*0.07391111*	*1.2×10^{-06}*	*0.07558154*	*0.07559086*	*9.32×10^{-06}*
2	*0.02865165*	*0.02866 41*	*1.2×10^{-05}*	*0.02954034*	*0.02955229*	*1.2×10^{-05}*	*0.03044838*	*0.03047164*	*2.3×10^{-05}*	*0.03137589*	*0.03140304*	*2.7 1×10^{-05}*
2.5	*0.01159765*	*0.01162016*	*2.2×10^{-05}*	*0.01205 05*	*0.01206 99*	*1.9×10^{-05}*	*0.01251683*	*0.01255143*	*3.4×10^{-05}*	*0.01299688*	*0.01303135*	*3.4 5×10^{-05}*
3	*0.00468487*	*0.00471711*	*3.2×10^{-05}*	*0.00490561*	*0.00492359*	*1.8×10^{-05}*	*0.00513467*	*0.00516291*	*2.8×10^{-05}*	*0.00537237*	*0.00539783*	*2.5 5×10^{-05}*
3.5	*0.00188 03*	*0.00191321*	*3.2×10^{-05}*	*0.00198409*	*0.00202162*	*3.7×10^{-05}*	*0.00209265*	*0.00214799*	*5.5×10^{-05}*	*0.00220628*	*0.00227316*	*6.6 9×10^{-05}*
4	*0.00073268*	*0.00073043*	*2.2×10^{-05}*	*0.00077899*	*0.00077721*	*1.7×10^{-06}*	*0.00082782*	*0.00082645*	*1.3×10^{-06}*	*0.00087955*	*0.00089826*	*1.8 7×10^{-05}*
4.5	*0.00024381*	*0.00022 8*	*1.5×10^{-05}*	*0.00026111*	*0.00024594*	*1.5×10^{-05}*	*0.00027949*	*0.00025693*	*2.2×10^{-05}*	*0.00029959*	*0.00026973*	*2.9 9×10^{-05}*
5	*-5.05E-07*	*-1.44E-05*	*1.39×10^{-05}*	*-6.16E-07*	*-2.11E-05*	*2.0×10^{-05}*	*-6.91E-07*	*-2.70E-05*	*2.6×10^{-05}*	3.71E-07	*-3.45E-05*	*3.4 9×10^{-05}*

The temperature profile $\theta(\eta)$, as a function of the melting parameter $M = 0.5,1,1.5,2,$ as shown in Table 3.

The independent variable η is listed in the first column. The RK-4 reference solutions are reported in the second, fifth, eighth, and eleventh columns, while the corresponding FFNN-BLMA predictions are provided in the third, sixth, ninth, and twelfth columns, respectively. This tabular comparison rigorously quantifies the influence of melting intensity on the thermal boundary layer and validates the predictive accuracy of the proposed neural network model across the selected parameter space.

Table 3. The $\theta(\eta)$ outputs of the proposed method for different M compared with the reference solutions.

$\theta(\eta)$	RK-4	BLMA	Error	RK-4	BLMA	Error	RK-4	BLMA	Error	RK-4	BLMA	Error
	M=0.5	M=0.5		M=1	M=1		M=1.5	M=1.5		M=2	M=2	
0	0	0.00011754	1.1754×10^-04	0	-1.58×10^-05	1.58×10^-05	0	-3.84×10^-05	3.84×10^-05	0	-1.41×10^-05	1.41×10^-05
0.5	0.52431829	0.52431229	6.00×10^-06	0.44169417	0.44169443	2.55×10^-07	0.38494959	0.38494699	2.60×10^-06	0.34310796	0.3431053	2.66×10^-06
1	0.80570399	0.80567637	2.76×10^-05	0.73020986	0.7302123	2.44×10^-06	0.66981282	0.66981612	3.30×10^-06	0.62056443	0.62056369	7.49×10^-07
1.5	0.92365978	0.92365953	2.57×10^-07	0.87629046	0.87629726	6.81×10^-06	0.83272577	0.83272665	8.78×10^-07	0.79366994	0.79367177	1.82×10^-06
2	0.96954434	0.9695106	3.37×10^-05	0.94343521	0.94342686	8.35×10^-06	0.91638423	0.91638129	2.94×10^-06	0.89003542	0.89003359	1.83×10^-06
2.5	0.98748841	0.98743749	5.09×10^-05	0.97378794	0.97377498	1.30×10^-05	0.95809228	0.95809667	4.39×10^-06	0.94168635	0.941688	1.65×10^-06
3	0.99474423	0.99468592	5.83×10^-05	0.98774489	0.98773791	6.98×10^-06	0.97901383	0.97901433	5.05×10^-07	0.96932732	0.96932713	1.90×10^-07
3.5	0.99779492	0.99770572	8.92×10^-05	0.99434616	0.99436384	1.77×10^-05	0.98972122	0.98972499	3.77×10^-06	0.98432574	0.98432556	1.82×10^-07
4	0.99912511	0.99909928	2.58×10^-05	0.99756251	0.99757666	1.41×10^-05	0.99533419	0.99533281	1.38×10^-06	0.99262239	0.99262337	9.82×10^-07
4.5	0.99972359	0.99976257	3.90×10^-05	0.99917337	0.99916622	7.15×10^-06	0.99834711	0.99834678	3.33×10^-07	0.99730538	0.99730418	1.20×10^-06
5	0.99999998	1.00005785	5.79×10^-05	0.99999997	0.99995295	4.70×10^-05	0.99999996	0.99998304	1.69×10^-05	0.99999996	0.99999699	2.97×10^-06

Table 4 displays the influence of the chemical reaction parameter γ = 0, 0.05, 0.1, 0.2, on the concentration profile $\phi(\eta)$. The independent variable η is listed in the first column. The RK-4 reference solutions are reported in the second, fifth, eighth, and eleventh columns, while the corresponding FFNN-BLMA predictions are presented in the third, sixth, ninth, and twelfth columns, respectively. This systematic comparison rigorously quantifies the consumptive effect of first-order chemical reactions on nanoparticle distribution and validates the predictive fidelity of the neural network across reactive regimes. Table 5 gives a detailed description of the architecture and evaluation methodology of the neural network utilized in the study. The network comprises three layers, where there is an input layer, one hidden layer of 10 neurons, and an output layer. A 10-fold cross-validation method is used to make sure that it is robust and general. There are 1000 points in the input and output grid, and the dataset is divided into training (70%), validation (15%), and testing (15%) subsets. In learning, the Levenberg-Marquardt algorithm is used. The target data to be used in training labels are generated using the RK-4 numerical method. Such a set-up will ensure that the functionality of the network is evaluated fairly and comprehensively. The legitimacy of the approach is reflected in every table that shows the correspondence of findings produced by the suggested soft computing scheme (BLMA) to the reference solutions (RK-4).

Table 4. The $\phi(\eta)$ outputs of the proposed method are compared with the reference solutions for different γ.

$\phi(\eta)$	RK-4	BLMA	Error	RK-4	BLMA	Error	RK-4	BLMA	Error	RK-4	BLMA	Error
	γ=0	γ=0		γ=0.05	γ=0.05		γ=0.1	γ=0.1		γ=0.2	γ=0.2	
0	0	3.70×10^-05	3.70×10^-05	0	-2.57×10^-06	2.57×10^-06	0	-1.49×10^-05	1.49×10^-05	0	7.06×10^-06	7.06×10^-06
0.5	0.7492353	0.74925344	1.81×10^-05	0.71514311	0.71514669	3.59×10^-06	0.68273505	0.68273432	7.33×10^-07	0.62261571	0.62262445	8.74×10^-06
1	0.9652649	0.96524852	1.80×10^-05	0.92573191	0.92572969	2.22×10^-06	0.88797755	0.88797802	4.69×10^-07	0.81746231	0.81746606	3.75×10^-06
1.5	0.9963206	0.99631962	1.24×10^-05	0.96082694	0.96082757	6.28E-07	0.92673122	0.92673124	9.59×10^-07	0.86252749	0.86252073	6.76×10^-06

2	*0.99965476*	*0.99962709*	*2.7 7×10^-05*	*0.969267 62*	*0.96928 317*	*1.5 5E-05*	*0.93992 728*	*0.93992 696*	*3.2 6×10^-07*	*0.88422 566*	*0.88422 181*	*3.8 5×10^-06*
2.5	*0.99996901*	*0.99998855*	*1.9 5×10^-05*	*0.974675 92ss*	*0.97469 154*	*1.5 6E-05*	*0.95012 464*	*0.95012 449*	*1.5 6×10^-07*	*0.90314 797*	*0.90314 663*	*1.3 3×10^-06*
3	*0.99999726*	*0.99999268*	*4.5 8×10^-06*	*0.979750 55*	*0.97975 769*	*7.1 4×10^-06*	*0.95999 559*	*0.95999 416*	*1.4 3×10^-06*	*0.92190 445*	*0.92190 776*	*3.3 1×10^-06*
3.5	*0.99999975*	*1.00000009*	*3.3 6×10^-07*	*0.984790 41*	*0.98478 357*	*6.8 5×10^-06*	*0.96987 415*	*0.96987 284*	*1.3 1×10^-06*	*0.94089 278*	*0.94089 904*	*6.2 7×10^-06*
4	*0.99999997*	*1.00000004*	*6.8 1×10^-08*	*0.989839 21*	*0.98983 009*	*9.1 2×10^-06*	*0.97982 321*	*0.97982 335*	*1.4 5×10^-07*	*0.96021 426*	*0.96022 077*	*6.5 1×10^-06*
4.5	*0.99999999*	*0.99999994*	*4.4 3×10^-08*	*0.994907 74*	*0.99490 994*	*2.2 1×10^-06*	*0.98986 237*	*0.98986 123*	*1.1 4×10^-06*	*0.97990 945*	*0.97990 335*	*6.0 9×10^-06*
5	*0.99999999*	*0.99999992*	*7.3 2×10^-08*	*0.999999 95*	*0.99994 709*	*5.2 9×10^-05*	*0.99999 99*	*0.99999 232*	*7.5 8×10^-06*	*0.99999 98*	*0.99997 542*	*2.4 4×10^-05*

Table 5. Structural and size data of the networks.

Parameters	***Description***
Layer structure	*One output, one input, and one hidden layer*
Hidden neuron	*10*
Validation	*10-fold cross-validation*
Input grid	*1000 points*
Output grid	*1000 points*
Training samples	*70%*
Validation samples	*15%*
Testing samples	*15%*
Learning methodology	*Levenberg-Marquardt*
Label target data	*Created with the RK-4 numerical method*

The distributions of temperature and velocity for various melting parameter values as shown in Figures 5 and 8. It is discovered that when M grows, the temperature distribution decreases while the boundary layer's thickness and velocity both rises. This is because an increase in M causes melting to occur with increased intensity, which serves as a boundary condition that blows at the stretched surface and thickens the boundary layer. Figure 11 shows how concentration profiles and chemical reaction parameters are related to one another. As the chemical reaction parameter increases, there is no discernible change in the fluid's temperature or velocity, but there is a decrease in the species concentration in the boundary layer. The chemical reaction that occurs in this system, which results in the chemical's consumption, is responsible for the decrease in the concentration profile. First-order chemical processes tend to lessen the overshoot in the profile of the solute concentration in the solutal boundary layer.

Figures 6, 9, and 12 display the efficacy examination graphs for each MLP network architecture. The inaccuracies were caused by differences between the reference and targeted solutions. The ANN design framework validates the correctness of the solution, as demonstrated by the graphical representation that shows how the intended outcome overlaps the reference artificial neural network (ANN) model outlines for models with different conditions. Determining the efficacy of ANN models requires analyzing the error histogram. The fitting of the approximate solution and the target data overlap, with relatively minor absolute errors, as shown in Figures 7, 10, and 13. The error histogram graphs show that each ANN model stage's mistakes are comparatively small. Even at this point, it is still clear that errors often accumulate around the zero-error line. Absolute error in the $f'(\eta)$, solutions are typically in the range of 10^{-5} to 10^{-6}, 10^{-5} to 10^{-6}, 10^{-4} to 10^{-7}, and 10^{-4} to 10^{-6}, respectively. The value range of the solution for $\theta(\eta)$, is approximately between 10^{-5} to 10^{-6}, 10^{-5} to 10^{-7}, 10^{-5} to 10^{-7}, and 10^{-5} to 10^{-8}, in that sequence. Similarly, the solution for $\phi(\eta)$, ranges between 10^{-5} to 10^{-7}, 10^{-5} to 10^{-7}, 10^{-5} to 10^{-7}, and 10^{-5} to 10^{-7}.

Figures 14, 15, and 16 collectively demonstrate the outstanding performance of the FFNN-BLMA in accurately predicting velocity $f'(\eta)$, temperature $\theta(\eta)$, and concentration $\phi(\eta)$, profiles compared to RK-4 reference solutions, with near-perfect curve overlap across all subfigures. As a melting parameter $M = 0$ to 2 increases, $f'(\eta)$, rises due to enhanced blowing and momentum boundary layer thickening, while $\theta(\eta)$, decreases from

intensified heat absorption and thermal layer thinning, similarly, as a chemical reaction parameter $\gamma = 0,$ to 0.2 rises, $\phi(\eta),$ declines due to species consumption, reducing solutal boundary layer thickness—trends precisely captured despite complex interactions involving thermal radiation, Brownian motion, and thermophoresis. Absolute errors range from 10^{-5} to 10^{-7} across all cases, with error histograms tightly clustered around zero, confirming exceptional precision, convergence, and reliability. This validates the novelty of FFNN-BLMA in efficiently solving highly nonlinear ODEs for non-Newtonian nanofluid flow without discretization, delivering superior accuracy, computational efficiency, and generalization over traditional numerical methods.

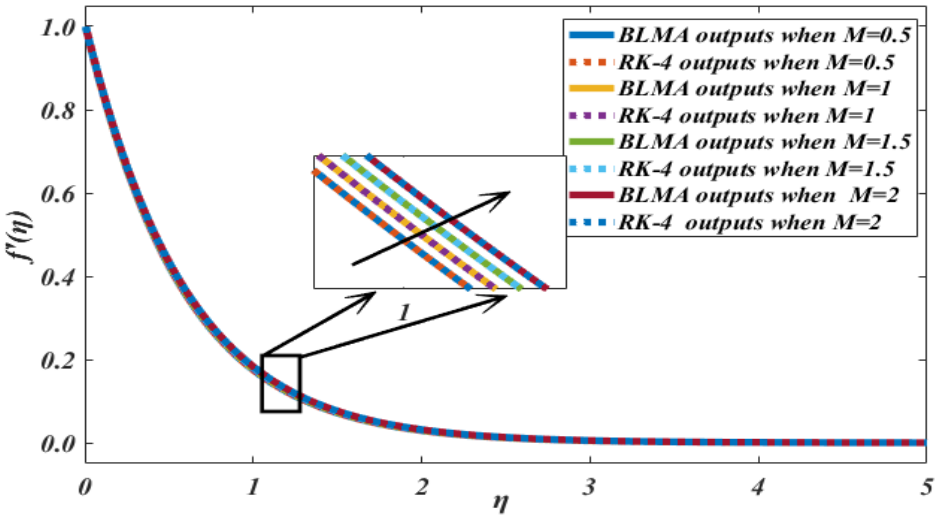

Figure 5. A numerical comparison with exact solutions in each case of $f'(\eta)$ using LMB neural networks in a complex analytic manner.

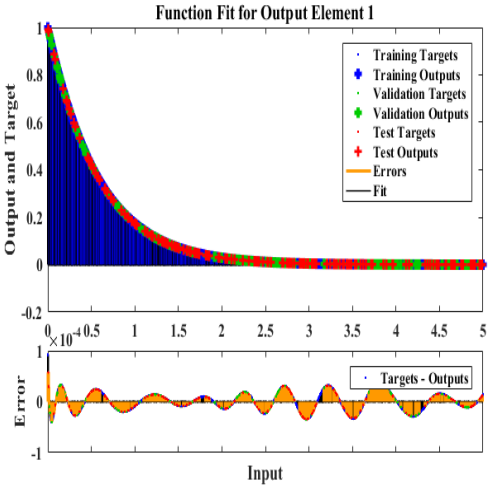

(a) Fitting graph at *M=0*

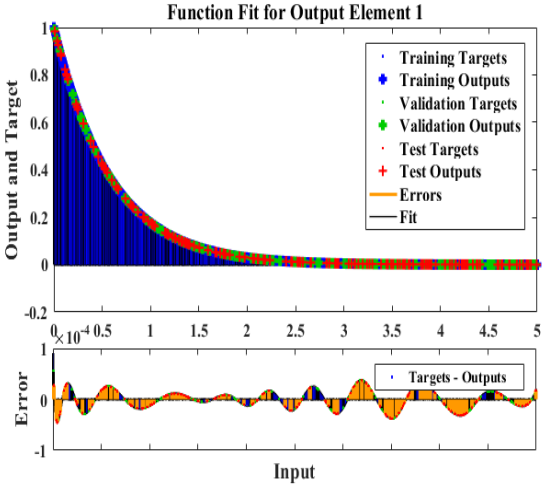

(b) Fitting graph at *M=0.5*

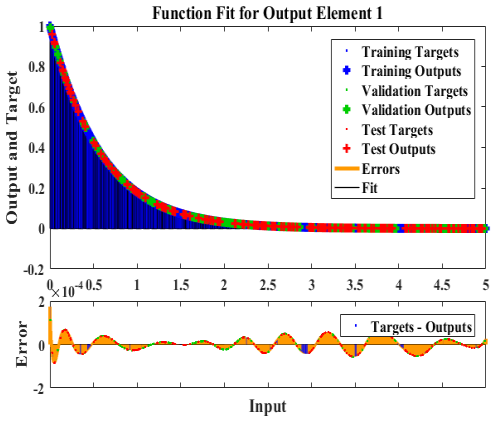

(c) Fitting graph at $M=1.5$

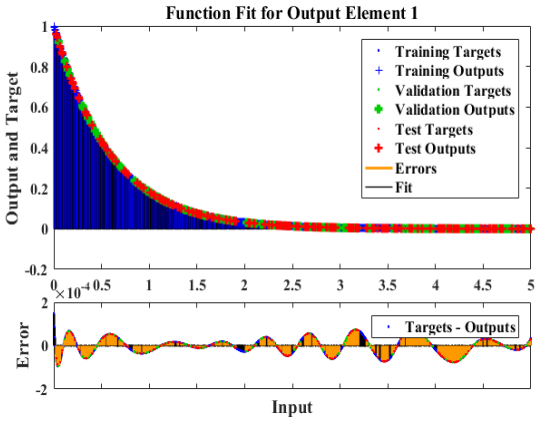

(d) Fitting graph at $M=2$

Figure 6. A comparison between LMB-NN numerical and approximate solutions for all cases of $f'(\eta)$.

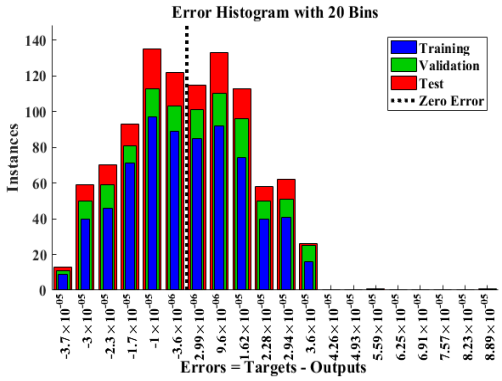

(a) The error histogram shows the error distribution when $M=0.5$

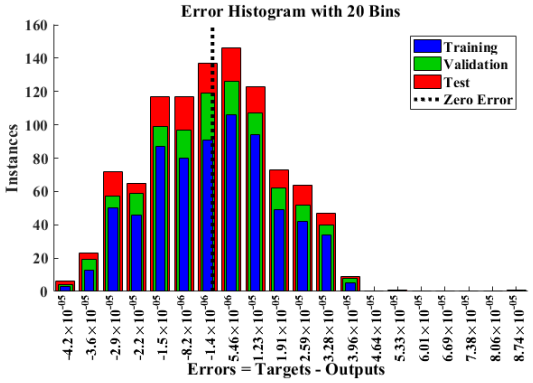

(b) Error histogram shows the error distribution when $M=1$

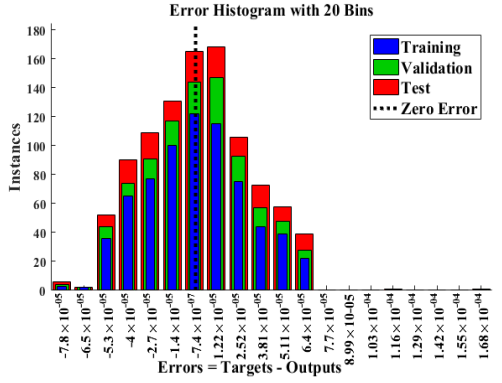

(c) The error histogram shows the error distribution when $M=1.5$

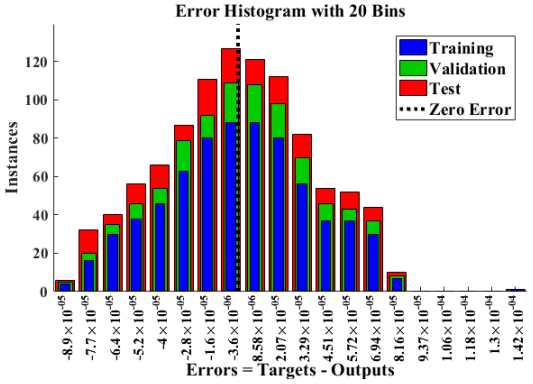

(d) Error histogram shows the error distribution when $M=2$

Figure 7. For each instance of $f'(\eta)$, there is a histogram showing the deviation of the predicted solutions from the actual data.

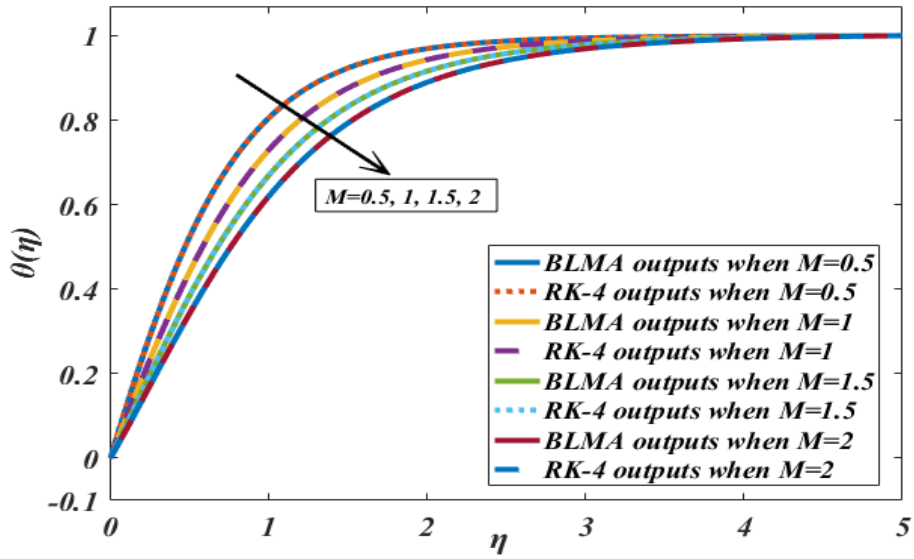

Figure 8. A comparative analysis with LMB-NN to provide an accurate solution for each case of *θ(η)*.

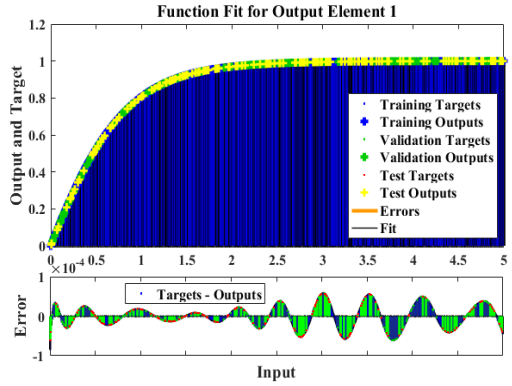

(a) Fitting graph at *M=0.5*

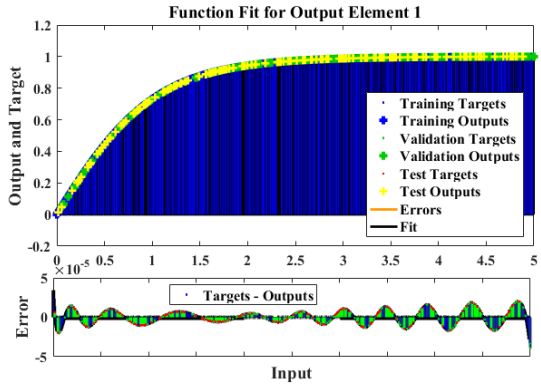

(b) Fitting graph at *M=1*

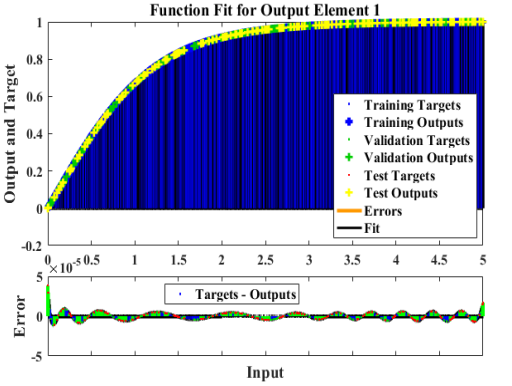

(c) Fitting graph at *M=1.5*

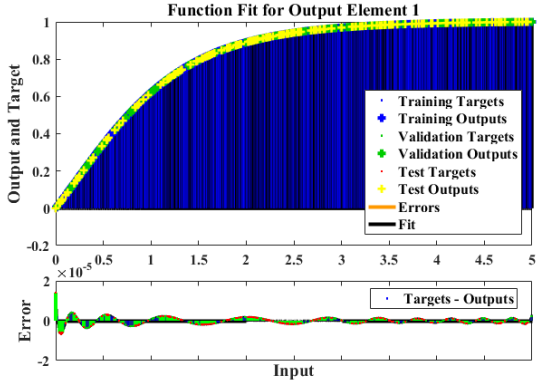

(d) Fitting graph at *M=2*

Figure 9. A comparison between LMB-NN numerical and approximate solutions for all cases of *θ(η)*.

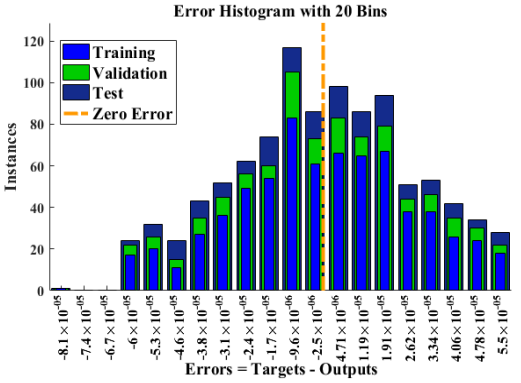

(a) Error histogram shows the error distribution when M=0.5

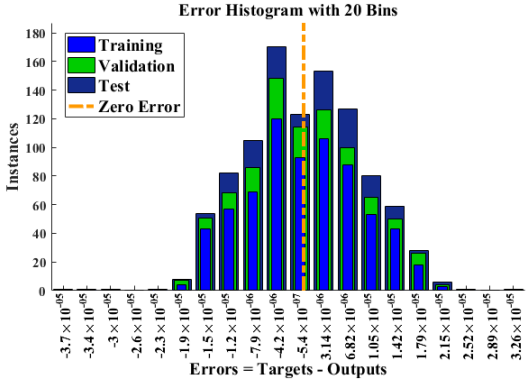

(b) Error histogram shows the error distribution when M=1

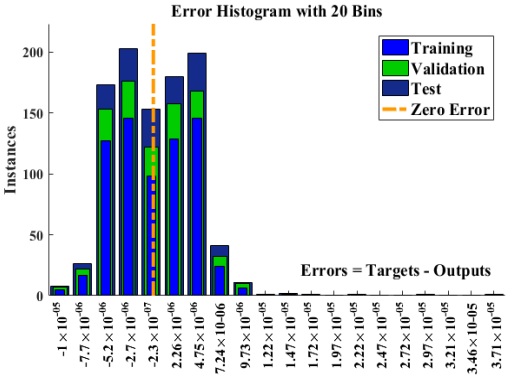

(c) The error histogram shows the error distribution when M=1.5

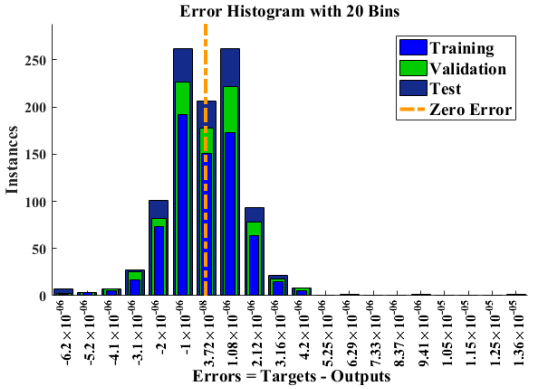

(d) Error histogram shows the error distribution when M=2

Figure 10. For each instance of $\theta(\eta)$, there is a histogram showing the deviation of the predicted solutions from the actual data.

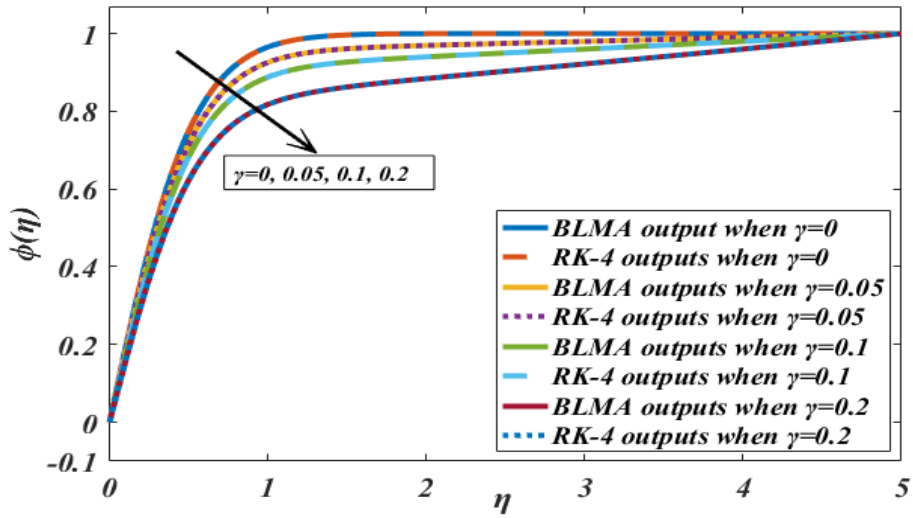

Figure 11. A comparative analysis with LMB-NN to provide an accurate solution for each case of $\phi(\eta)$.

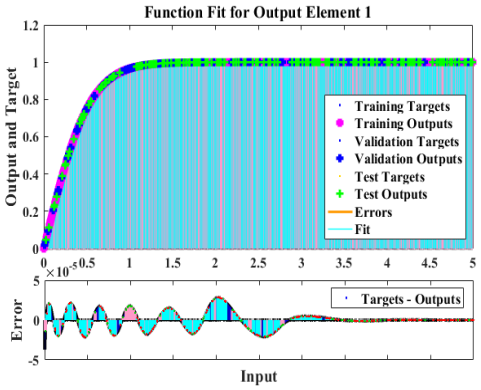

(a) Fitting the graph at $\gamma=0$

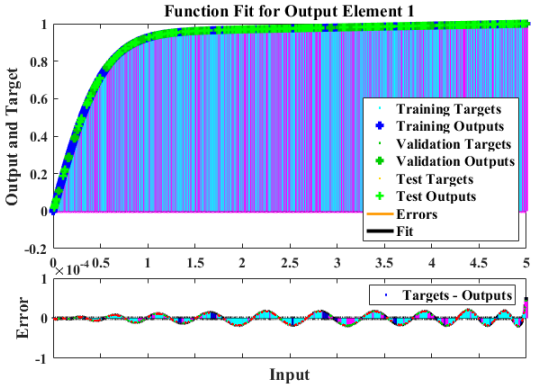

(b) Fitting graph at $\gamma=0.05$

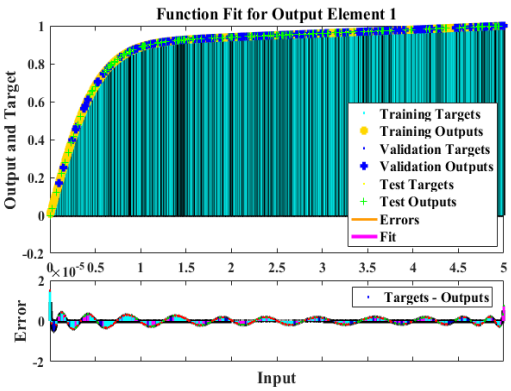

(c) Fitting the graph at $\gamma=0.1$

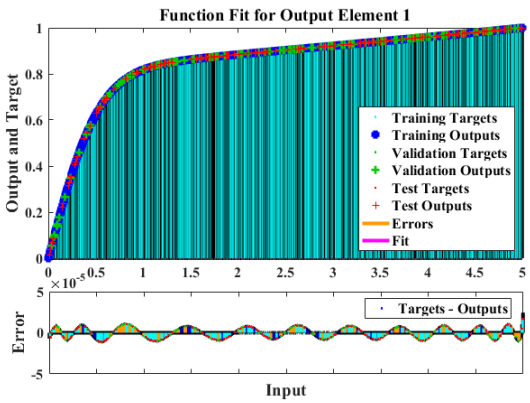

(d) Fitting graph at $\gamma=0.2$

Figure 12. A comparison between LMB-NN numerical and approximate solutions for all cases of $\phi(\eta)$.

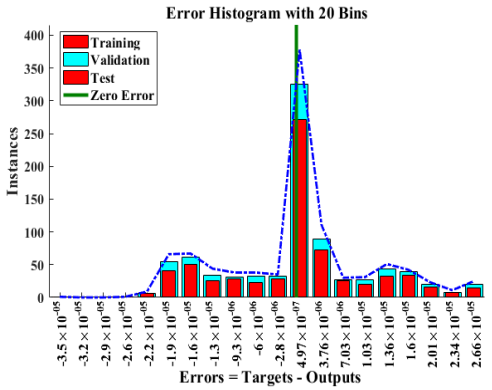

(a) The error histogram shows the error distribution when $\gamma=0$

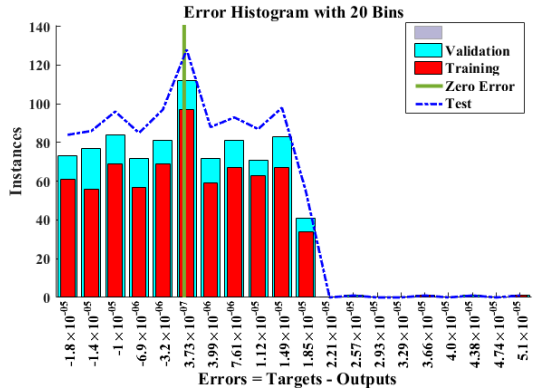

(b) Error histogram shows the error distribution when $\gamma=0.05$

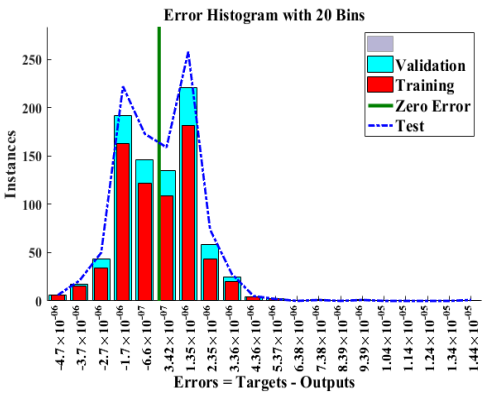

(c) The error histogram shows the error distribution when γ=0.1

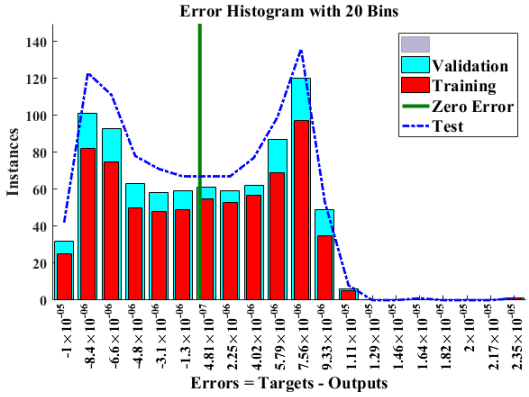

(d) Error histogram shows the error distribution when γ=0.2

Figure 13. For each instance of $\phi(\eta)$, there is a histogram showing the deviation of the predicted solutions from the actual data.

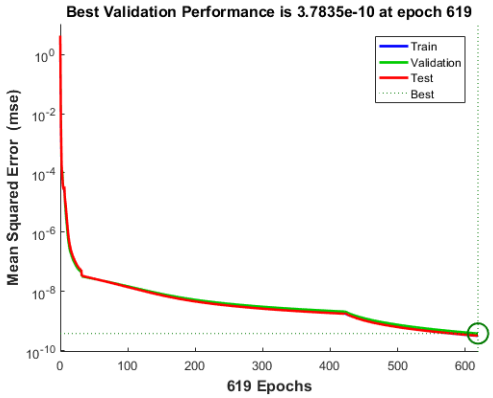

(a) Performance graph at *M=0*

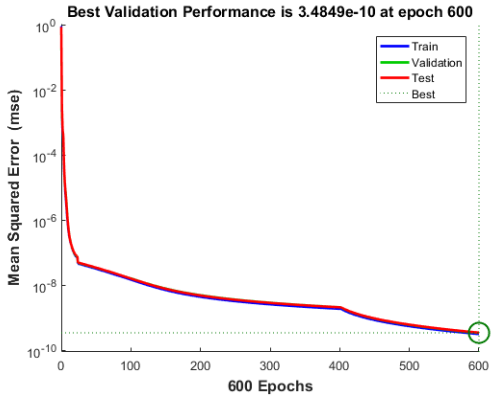

(b) Performance graph at *M=1*

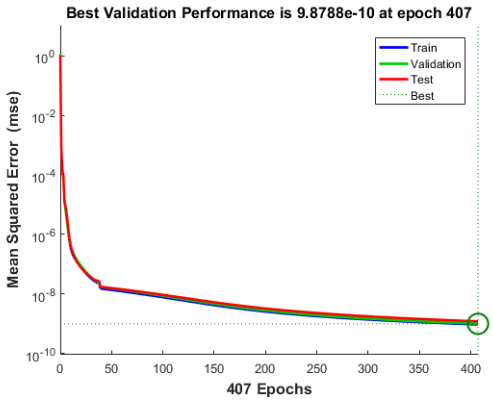

(c) Performance graph at *M=1.5*

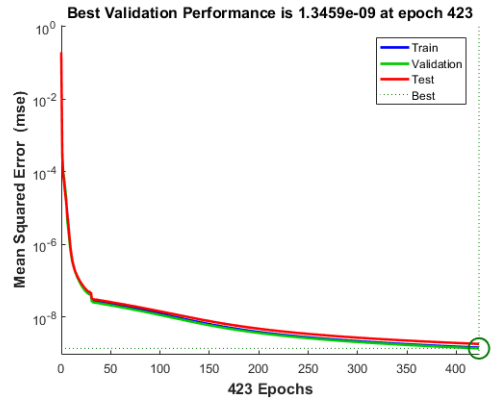

(d) Performance graph at *M=2*

Figure 14. Velocity profile *f'(η)* comparison between RK-4 and BLMA at M=0, 1, 1.5, and 2.

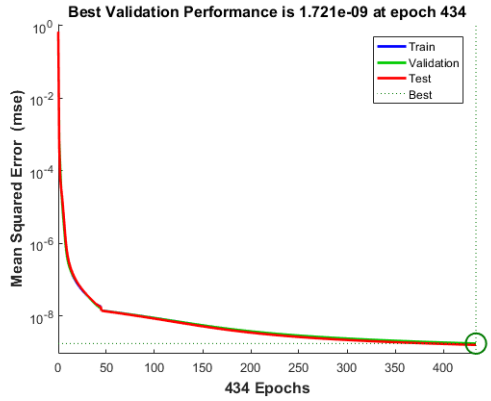

(a) Performance graph at *M=0*

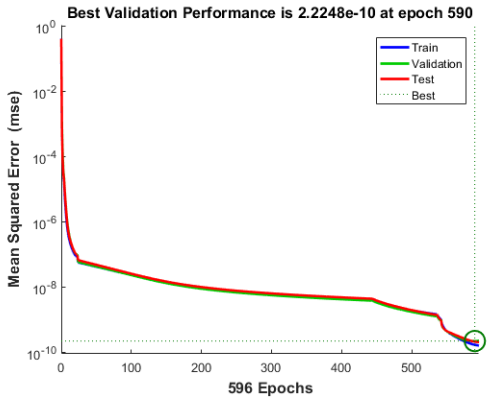

(b) Performance graph at *M=1*

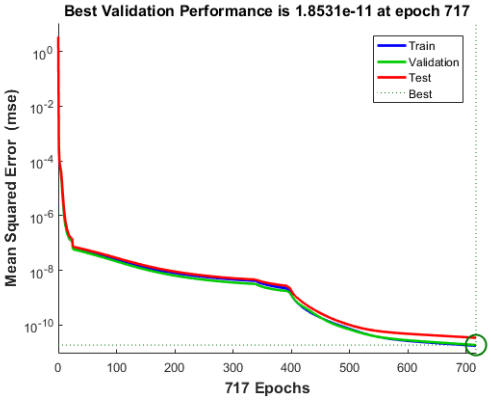

(c) Performance graph at *M=1.5*

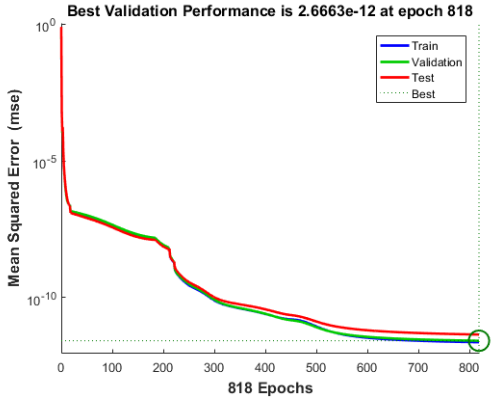

(d) Performance graph at *M=2*

Figure 15. Temperature profile *θ(η)* comparison between RK-4 and BLMA at M=0, 1, 1.5, and 2.

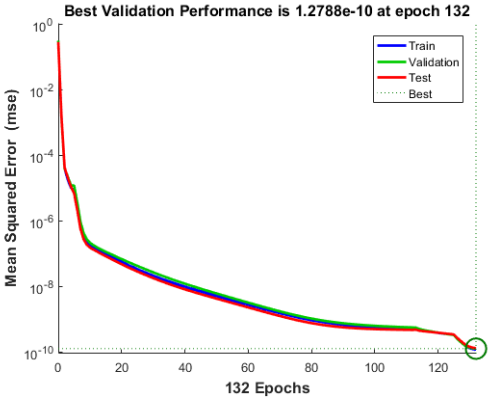

(a) Performance graph at *γ=0*

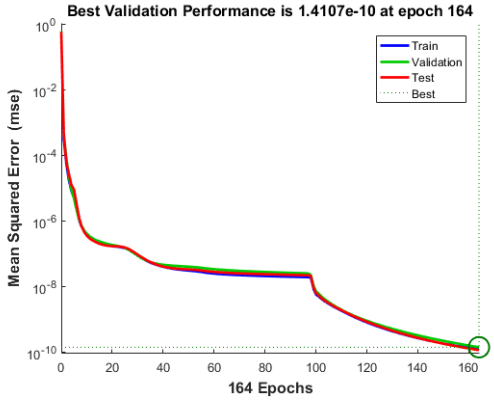

(b) Performance graph at *γ=0.05*

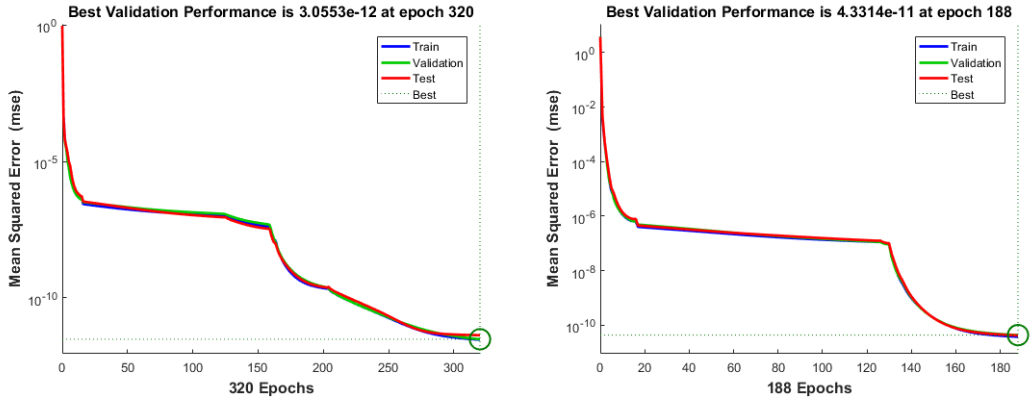

(c) Performance graph at γ=0.1 **(d) Performance graph at γ=0.2**

Figure 16. Concentration profile $\phi(\eta)$ comparison between RK-4 and BLMA at γ=0, 0.05, 0.1, and 0.2.

6. Conclusion

The current research implemented a numerical and machine learning approach to examine the melting, radiation, and chemical reaction effects on the steady boundary layer flow of a Williamson nanofluid over a horizontally linearly stretching sheet embedded in a porous medium. The transformed nonlinear ordinary differential equations governing the flow were solved using the Runge–Kutta fourth order (RK-4) method to generate high-fidelity reference data, which trained a supervised Feed-Forward Neural Network optimized via the Backpropagated Levenberg-Marquardt Algorithm (FFNN-BLMA). This hybrid methodology achieved exceptional predictive accuracy with absolute errors ranging from 10^{-8} to 10^{-10} across velocity, temperature, and concentration profiles, validated through 10-fold cross-validation, mean squared error minimization, regression analysis, and error histograms.

Key physical insights reveal that increasing the melting parameter M enhances velocity and thermal boundary layer thickness while reducing temperature; conversely, a higher chemical reaction parameter γ significantly suppresses species concentration due to consumptive reactions, with minimal influence on thermal and momentum fields. The FFNN-BLMA technique demonstrates superior convergence, computational efficiency, and robustness compared to standalone numerical schemes, eliminating the need for discretization, mesh refinement, or differentiability assumptions, making it ideally suited for stiff, multi-physics, non-Newtonian systems.

Future applications of the proposed FFNN-BLMA framework extend beyond integer-order ODEs to fractional-order partial differential equations, time-dependent viscoelastic flows, multi-phase nanofluid dynamics, and real-time control in thermal engineering systems, paving the way for AI-driven predictive modeling in advanced materials processing, energy systems, and biomedical fluid mechanics.

Acknowledgment

This study is supported via funding from Prince Sattam bin Abdulaziz University project number (PSAU/2025/R/1447).

References

[1] J. Zeng, Y. Xuan, Analysis on interaction between solar light and suspended nanoparticles in nanofluids, *Journal of Quantitative Spectroscopy and Radiative Transfer,* Vol. 269, pp. 107692, 2021.

[2] A. M. Alqahtani, M. Bilal, M. Usman, T. R. Alsenani, A. Ali, S. R. Mahmuod, Heat and mass transfer through MHD Darcy Forchheimer Casson hybrid nanofluid flow across an exponential stretching sheet, *ZAMM-Journal of Applied Mathematics and Mechanics/Zeitschrift für Angewandte Mathematik und Mechanik,* Vol. 103, No. 6, pp. e202200213, 2023.

[3] M. F. Endalew, S. Sarkar, Numerical exploration of forced convection hydromagnetic hyperbolic tangent nanofluid flow over a permeable wedge with melting heat transfer, *Scientific Reports,* Vol. 13, No. 1, pp. 3515, 2023.

[4] F. Mabood, G. Bognár, A. Shafiq, Impact of heat generation/absorption of magnetohydrodynamics Oldroyd-B fluid impinging on an inclined stretching sheet with radiation, *Scientific Reports,* Vol. 10, No. 1, pp. 17688, 2020.

[5] A. M Megahed, Williamson fluid flow due to a nonlinearly stretching sheet with viscous dissipation and thermal radiation, *Journal of the Egyptian Mathematical Society,* Vol. 27, No. 1, pp. 1-10, 2019.

[6] S. Parvin, S. S. P. Mohamed Isa, N. M. Arifin, F. Md Ali, The inclined factors of magnetic field and shrinking sheet in Casson fluid flow, heat and mass transfer, *Symmetry,* Vol. 13, No. 3, pp. 373, 2021.

[7] H. Maaitah, A. N. Olimat, O. Quran, H. M. Duwairi, Viscous dissipation analysis of Williamson fluid over a horizontal saturated porous plate at constant wall temperature, *International Journal of Thermofluids,* Vol. 19, pp. 100361, 2023.

[8] Z. Khan, A. Ali, S. Aldahmani, H. Nordmark, B. Lausen, Customer lifetime value modelling via two stage selected trees ensembles, *IEEE Access*, 2025.

[9] S. Gul, D. Muhammad Khan, S. Aldahmani, Z. Khan, Margin weighted robust discriminant score for feature selection in imbalanced gene expression classification, *PLoS One,* Vol. 20, No. 6, pp. e0325147, 2025.

[10] M. R. Khan, M. A. Elkotb, R. Matoog, N. A. Alshehri, M. A. Abdelmohimen, Thermal features and heat transfer enhancement of a Casson fluid across a porous stretching/shrinking sheet: Analysis of dual solutions, *Case Studies in Thermal Engineering,* Vol. 28, pp. 101594, 2021.

[11] A. Ali, Z. Khan, H. Du, S. Aldahmani, Double weighted k nearest neighbours for binary classification of high dimensional genomic data, *Scientific reports,* Vol. 15, No. 1, pp. 12681, 2025.

[12] A. Ali, Z. Khan, S. Aldahmani, Optimized feature selection in high-dimensional gene expression data using weighted differential gene expression analysis, *Applied Soft Computing*, pp. 113329, 2025.

[13] K. Prasad, H. Vaidya, K. Vajravelu, G. Manjunatha, M. Rahimi-Gorji, H. Basha, Heat transfer analysis of three-dimensional mixed convective flow of an oldroyd-B nanoliquid over a slippery stretching surface, in *Proceeding of,* Trans Tech Publ*,* pp. 164-182.

[14] Z. Khan, A. Ali, D. M. Khan, S. Aldahmani, Regularized ensemble learning for prediction and risk factors assessment of students at risk in the post-COVID era, *Scientific reports,* Vol. 14, No. 1, pp. 16200, 2024.

[15] Z. Khan, A. Ali, S. Aldahmani, Feature selection via robust weighted score for high dimensional binary class-imbalanced gene expression data, *Heliyon,* Vol. 10, No. 19, 2024.

[16] E. O. Titiloye, J. A. Gbadeyan, A. T. Adeosun, Heat and mass transfer of MHD dissipative Casson nanofluid flow over a stretching or shrinking sheet with multiple slip boundary conditions, in *Proceeding of,* Trans Tech Publ*,* pp. 103-120.

[17] A. Ali, Z. Khan, D. M. Khan, S. Aldahmani, An optimal random projection k nearest neighbors ensemble via extended neighborhood rule for binary classification, *IEEE Access,* Vol. 12, pp. 61401-61409, 2024.

[18] S. Aldahmani, O. Kortbi, M. Mesfioui, Copula-Based Regression with Mixed Covariates, *Mathematics,* Vol. 12, No. 22, pp. 3525, 2024.

[19] B. Gireesha, M. Umeshaiah, B. Prasannakumara, N. Shashikumar, M. Archana, Impact of nonlinear thermal radiation on magnetohydrodynamic three dimensional boundary layer flow of Jeffrey nanofluid over a nonlinearly permeable stretching sheet, *Physica A: Statistical Mechanics and its Applications,* Vol. 549, pp. 124051, 2020.

[20] M. Hamraz, A. Ali, W. K. Mashwani, S. Aldahmani, Z. Khan, Feature selection for high dimensional microarray gene expression data via weighted signal to noise ratio, *PloS one,* Vol. 18, No. 4, pp. e0284619, 2023.

[21] N. Gul, W. K. Mashwani, M. Aamir, S. Aldahmani, Z. Khan, Optimal model selection for k-nearest neighbours ensemble via sub-bagging and sub-sampling with feature weighting, *Alexandria Engineering Journal,* Vol. 72, pp. 157-168, 2023.

[22] S. Shehzad, T. Hayat, A. Alsaedi, MHD flow of Jeffrey nanofluid with convective boundary conditions, *Journal of the Brazilian Society of Mechanical Sciences and Engineering,* Vol. 37, No. 3, pp. 873-883, 2015.

[23] A. Ali, M. Hamraz, N. Gul, D. M. Khan, S. Aldahmani, Z. Khan, A k nearest neighbour ensemble via extended neighbourhood rule and feature subsets, *Pattern Recognition,* Vol. 142, pp. 109641, 2023.

[24] R. Abdullah Mohamed, A. Mahmoud Aly, S. Elsayed Ahmed, M. Sayed Soliman, MHD Jeffrey nanofluids flow over a stretching sheet through a porous medium in presence of nonlinear thermal radiation and heat generation/absorption, *Challenges in Nano and Micro Scale Science and Technology,* Vol. 8, No. 1, pp. 9-22, 2020.

[25] N. Younas, A. Ali, H. Hina, M. Hamraz, Z. Khan, S. Aldahmani, Optimal causal decision trees ensemble for improved prediction and causal inference, *IEEE Access,* Vol. 10, pp. 13000-13011, 2022.

[26] M. Hamraz, Z. Khan, D. M. Khan, N. Gul, A. Ali, S. Aldahmani, Gene selection in binary classification problems within functional genomics experiments via robust Fisher score, *IEEE Access,* Vol. 10, pp. 51682-51692, 2022.

[27] D.-C. Lu, M. Ramzan, M. Bilal, J. D. Chung, U. Farooq, Upshot of chemical species and nonlinear thermal radiation on Oldroyd-B nanofluid flow past a bi-directional stretched surface with heat generation/absorption in a porous media, *Communications in Theoretical Physics,* Vol. 70, No. 1, pp. 071, 2018.

[28] N. Gul, M. Aamir, S. Aldahmani, Z. Khan, A weighted k-Nearest neighbours ensemble with added accuracy and diversity, *IEEE Access,* Vol. 10, pp. 125920-125929, 2022.

[29] T. Hayat, M. B. Ashraf, S. Shehzad, N. N. Bayomi, Mixed convection flow of viscoelastic nanofluid over a stretching cylinder, *Journal of the Brazilian Society of Mechanical Sciences and Engineering,* Vol. 37, No. 3, pp. 849-859, 2015.

[30] Z. Khan, M. Naeem, U. Khalil, D. M. Khan, S. Aldahmani, M. Hamraz, Feature selection for binary classification within functional genomics experiments via interquartile range and clustering, *IEEE Access,* Vol. 7, pp. 78159-78169, 2019.

[31] Y. B. Kho, A. Hussanan, M. K. A. Mohamed, M. Z. Salleh, Heat and mass transfer analysis on flow of Williamson nanofluid with thermal and velocity slips: Buongiorno model, *Propulsion and Power Research,* Vol. 8, No. 3, pp. 243-252, 2019.

[32] S. Aldahmani, H. Dai, Q.-Z. Zhang, Hybrid Graphical Least Square estimation and its application in portfolio selection, *Statistics and Its Interface,* Vol. 12, No. 4, pp. 631-645, 2019.

[33] K. Swain, S. M. Ibrahim, G. Dharmaiah, S. Noeiaghdam, Numerical study of nanoparticles aggregation on radiative 3D flow of maxwell fluid over a permeable stretching surface with thermal radiation and heat source/sink, *Results in Engineering,* Vol. 19, pp. 101208, 2023.

[34] K. Ren, G. Wu, G. Thomas, Wave excited motion of a body floating on water confined between two semi-infinite ice sheets, *Physics of Fluids,* Vol. 28, No. 12, 2016.

[35] J. H. Lienhard, Heat transfer in flat-plate boundary layers: A correlation for laminar, transitional, and turbulent flow, *Journal of Heat Transfer,* Vol. 142, No. 6, pp. 061805, 2020.

[36] R. Sharma, N. Acharya, K. Das, On the impact of variable thickness and melting transfer of heat on magnetohydrodynamics nanofluid flow past a slendering stretching sheet, *Indian J. Geo-Mar. Sci,* Vol. 49, pp. 641-648, 2020.

[37] B. Prasannakumara, B. Gireesha, P. Manjunatha, Melting phenomenon in MHD stagnation point flow of dusty fluid over a stretching sheet in the presence of thermal radiation and non-uniform heat source/sink, *International Journal for Computational Methods in Engineering Science and Mechanics,* Vol. 16, No. 5, pp. 265-274, 2015.

[38] S. Hasan, *Numerical Investigation of Convective Heat and Mass Transfer Flow along a Vertical Porous Plate with Soret and Dufour Effects in the Presence of Induced Magnetic Field*, Thesis, Khulna University of Engineering & Technology (KUET), Khulna, Bangladesh., 2017.

[39] A. K. Dash, S. Mishra, MHD stagnation point flow of micropolar fluid past on a vertical plate in the presence of porous medium, *European Journal of Electrical Engineering,* Vol. 19, No. 1-2, pp. 43, 2017.

[40] D. Sahu, R. K. Deka, Influences of thermal stratification and chemical reaction on MHD free convective flow along an accelerated vertical plate with variable temperature and exponential mass diffusion in a porous medium, *Heat Transfer,* Vol. 53, No. 7, pp. 3643-3666, 2024.

[41] Z. Lv, L. Qiao, J. Li, H. Song, Deep-learning-enabled security issues in the internet of things, *IEEE Internet of Things Journal,* Vol. 8, No. 12, pp. 9531-9538, 2020.

[42] D. Pal, G. Mandal, Mixed convection–radiation on stagnation-point flow of nanofluids over a stretching/shrinking sheet in a porous medium with heat generation and viscous dissipation, *Journal of Petroleum Science and Engineering,* Vol. 126, pp. 16-25, 2015.

[43] G. S. Seth, R. Tripathi, M. Rashidi, Hydromagnetic natural convection flow in a non-Darcy medium with Soret and Dufour effects past an inclined stretching sheet, *Journal of Porous Media,* Vol. 20, No. 10, 2017.

[44] N. A. Khan, M. Sulaiman, F. S. Alshammari, Heat transfer analysis of an inclined longitudinal porous fin of trapezoidal, rectangular and dovetail profiles using cascade neural networks, *Structural and Multidisciplinary Optimization,* Vol. 65, No. 9, pp. 251, 2022.

[45] M. Sulaiman, Z. Hussain, F. S. Alshammari, G. Laouin, Computational Analysis of Natural Convection Heat Transfer in Nanofluids Under a Uniform Magnetic Field Using Levenberg–Marquardt Backpropagation Neural Networks, *Journal of Computational Applied Mechanics,* Vol. 57, No. 1, pp. 41-62, 2026.

[46] N. Sharif, M. Alam, H. U. Molla, Dynamics of nonlinear pendulum equations: Modified homotopy perturbation method, *Journal of Low Frequency Noise, Vibration and Active Control,* Vol. 44, No. 3, pp. 1460-1473, 2025.

[47] H. Y. Lam, G. Ceruti, D. Kressner, Randomize Low-Rank Runge–Kutta Methods, *SIAM Journal on Matrix Analysis and Applications,* Vol. 46, No. 2, pp. 1587-1615, 2025.

[48] A. Khan, M. Sulaiman, H. Alhakami, A. Alhindi, Analysis of oscillatory behavior of heart by using a novel neuroevolutionary approach, *IEEE Access,* Vol. 8, pp. 86674-86695, 2020.

[49] T. Demir, Unified Theory and Intelligent Simulation Platform for Coupled Multi-Physics, Multi-Scale, and Fractional-Order Systems: Foundations, Algorithms, and Digital Twin Applications.

[50] M. Sulaiman, M. Masihullah, Z. Hussain, S. Ahmad, W. K. Mashwani, M. A. Jan, R. A. Khanum, Implementation of improved grasshopper optimization algorithm to solve economic load dispatch problems, *Hacettepe Journal of Mathematics and Statistics,* Vol. 48, No. 5, pp. 1570-1589, 2019.

[51] R. Kumar, R. Mehta, A. Bhatnagar, I. Ozsahin, B. Uzun, B. Almohsen, H. Ahmad, Numerical study of Williamson fluid flow over a stretching sheet with Newtonian heating embedded in a porous medium in presence of thermal radiation and heat source/sink, *Journal of Nonlinear Mathematical Physics,* Vol. 32, No. 1, pp. 4, 2025.

[52] M. Krishnamurthy, B. Prasannakumara, B. Gireesha, R. S. R. Gorla, Effect of chemical reaction on MHD boundary layer flow and melting heat transfer of Williamson nanofluid in porous medium, *Engineering Science and Technology, an International Journal,* Vol. 19, No. 1, pp. 53-61, 2016.